A Journal of the Gesellschaft Deutscher Chemiker

Angewandte International Edition GDCh Chemie

www.angewandte.org

Accepted Article

Title: CoN1O2 Single-Atom Catalyst for Efficient Peroxymonosulfate Activation and Selective Cobalt(IV)=O Generation

Authors: Xue Li, Xue Wen, Junyu Lang, Yan Wei, Jie Miao, Xiangcheng Zhang, Baoxue Zhou, Mingce Long, Pedro J. J. Alvarez, and Lizhi Zhang

To be cited as: *Angew. Chem. Int. Ed.* **2023**, e202303267

Link to VoR: https://doi.org/10.1002/anie.202303267

WILEY VCH

10.1002/anie.202303267

WILEY-VCH

RESEARCH ARTICLE

CoN_1O_2 Single-Atom Catalyst for Efficient Peroxymonosulfate Activation and Selective Cobalt$^{(IV)}$=O Generation

Xue Li, [a] Xue Wen, [a] Junyu Lang, [b] Yan Wei, [a] Jie Miao, [a] Xiangcheng Zhang, [a] Baoxue Zhou, [a] Mingce Long, *[a] Pedro J. J. Alvarez, [c] and Lizhi Zhang *[a]

[a] X. Li, X. Wen, Y. Wei, J. Miao, X. C. Zhang, B. X. Zhou, Prof. Dr. M. C. Long, Prof. Dr. L. Z. Zhang
School of Environmental Science and Engineering, Key Laboratory of Thin Film and Microfabrication Technology (Ministry of Education)
Shanghai Jiao Tong University
Shanghai 200240, P. R. China
E-mail: long_mc@sjtu.edu.cn (M. C. Long) and zhanglizhi@sjtu.edu.cn (L. Z. Zhang)
[b] Prof. Dr. J. Y. Lang
School of Physical Science and Technology
Shanghai Tech University
Shanghai 201210, P. R. China
[c] Prof. Dr. Pedro J. J. Alvarez
Department of Civil and Environmental Engineering
Rice University
Houston TX 77005, United States

Supporting information for this article is given via a link at the end of the document.

Abstract: High-valent metal-oxo (HVMO) are powerful non-radical reactive species that enhance advanced oxidation processes (AOPs) due to their long half-lives and high selectivity towards recalcitrant water pollutants with electron-donating groups. However, high-valent cobalt-oxo (Co^{IV}=O) generation is challenging in peroxymonosulfate (PMS)-based AOPs because the high 3d-orbital occupancy of cobalt would disfavour its binding with a terminal oxygen ligand. Herein, we propose a strategy to construct isolated Co sites with unique N_1O_2 coordination on Mn_3O_4 surface. The asymmetric N_1O_2 configuration is able to accept electrons from Co 3d-orbital, resulting in significant electronic delocalization at Co sites for the promoted PMS adsorption, dissociation and subsequent generation of Co^{IV}=O species. CoN_1O_2/Mn_3O_4 exhibits high intrinsic activity in PMS activation and sulfamethoxazole (SMX) degradation, highly outperforming its counterpart with CoO_3 configuration, carbon-based single-atom catalysts with CoN_4 configuration, and commercial cobalt oxides. Co^{IV}=O species effectively oxidize the target contaminants via oxygen atom transfer to produce low-toxicity intermediates. These findings could advance mechanistic understanding of PMS activation at the molecular level and guide the rational design of efficient environmental catalysts.

Introduction

Peroxymonosulfate (PMS)-based advanced oxidation processes (AOPs) are amongst the most promising technologies to degrade recalcitrant organic pollutants in water.[1] Developing efficient catalysts to active PMS and produce reactive species is crucial to accelerate organic pollutant oxidation. Among homogeneous first-row transition-metal (Co^{2+}, Fe^{2+}, Cu^{2+}, and Mn^{2+}) catalysts, cobalt ion is one of the most active one for PMS activation to produce free radicals ($SO_4^{\bullet-}$ and •OH), but it suffers from unfeasible recyclability.[2] Thus, heterogeneous cobalt-based catalysts for PMS activation have been extensively explored,[3] and cobalt single-atom catalysts (SACs) are recently emerging as the most promising candidate due to their utmost atom utilization efficiencies and tunable electronic structures.

Many carbon-based SACs have been developed with nitrogen-coordinated Co configurations like CoN_4, CoN_{2+2}, and CoN_2. These SACs have been demonstrated to be efficient for $^1O_2$-dominated PMS activation.[1b, 4] However, little attention has been given to generating high-valent cobalt-oxo (Co^{IV}=O) species by modulating Co configurations in the SACs.[5] Generally, high-valent metal-oxo (HVMO) species offer the advantages of long lifetimes (7-10^{-1} s >> 10^{-6}-10^{-9} s for radicals), high steady-state concentrations (~10^{-8} M >> 10^{-12}-10^{-15} M for radicals), and less susceptibility to scavenging by non-target substrates (e.g. natural organic matter). Furthermore, Co^{IV}=O has higher oxidation potential than the counterparts (Fe^{IV}=O and Mn^{IV}=O). Thus, it is important to develop catalysts that produce Co^{IV}=O species during PMS activation.[6]

The difficulty to generate Co^{IV}=O is due to the well-known "oxo wall" rule for the late-transition-metals; that is, the high d-orbital occupancy with more than four electrons (five for Co (IV)) hinders bonding with a terminal oxygen ligand, and the metal-oxo π-bond order would also be less than one.[7] Encouragingly, Co^{IV}=O species were detected in the Co (II)/PMS system under acidic pH conditions, suggesting the feasibility of Co^{IV}=O generation in PMS activation.[2, 8] However, homogeneous Co^{IV}=O are extremely susceptible to conversion to Co (III) due to strong electronic repulsion between the cobalt center and the electron-rich oxygen atom.[7c] To fundamentally overcome the difficulties in generating Co^{IV}=O species, it is essential to reduce the 3d-orbital

filling of cobalt and to liberate orbitals to host electrons from oxygen donors.[7a, 9] This has been achieved by optimizing the ligands and enhancing the spin-states of cobalt in a few enzyme-like cobalt (IV)-oxo complexes, which are successfully applied in cobalt-mediated alkane hydroxylation and dioxygen four-electron reduction reactions.[10] Inspired by these complexes, and considering the strong interactions between transition metal (TM) centers and ligands in SACs that influence d-orbital occupancy in the central atoms, a rational design of the coordination structure of TM centers could mitigate the high d-orbital occupancy of TM centers in SACs.[11] In fact, reduced d-orbital filling of TM centers was observed in a CoN_4 planar structure with an axial O ligand, in which oxygen can axially extract a fraction of electrons from Co 3d-orbital, causing electronic delocalization at Co sites.[9a] Similar results were also found in the Ni-based SACs with axial O ligand.[12] Thus, we anticipate to extract electrons from the metal d-orbital by asymmetrically co-coordinating with nitrogen and oxygen, and accordingly favoring Co^{IV}=O generation during PMS activation.

To fabricate isolated Co sites with well-defined coordination, metal oxides such as spinel Mn_3O_4 with exact crystal structures have an advantage over carbon-based materials, which always result in undefined coordination in SACs due to the inherent uncontrollable pyrolysis.[4, 13] In this work, a CoN_1O_2 configuration was constructed on spinel Mn_3O_4 surface. We demonstrate efficient activity for PMS activation and exclusive production of Co^{IV}=O species, and discern the mechanism of heterogeneous Co^{IV}=O species formation via PMS activation. Thus, this study not only provides a feasible strategy for the heterogeneous Co^{IV}=O species formation, but also advances fundamental understanding of oxide-based SACs design at the atomic level.

Results and Discussion

CoN_1O_2/Mn_3O_4 was synthesized through a reverse atom-trapping strategy (**Figure 1a**), in which single Mn atoms were extracted from the rigid Mn_3O_4 surface to form manganese chloride crystals during ammonium chloride-mediated calcination (**Figure S1**), and the formed manganese chloride was easily removed by water washing.[14] Then, the single Co atoms from thermal decomposition of cobalt acetylacetonate occupied the defective Mn sites. The ammonia atmosphere from ammonium chloride pyrolysis served as nitrogen source to adjust the coordination environment of isolated Co atoms. Eventually, a catalyst with Co and N anchoring over rigid Mn_3O_4 surface with atomic precision was obtained. The control samples without N (denoted as Co/Mn_3O_4) or Co atoms (denoted as N/Mn_3O_4) was also prepared by the same procedure, but without ammonium chloride and cobalt acetylacetonate, respectively.

The as-prepared CoN_1O_2/Mn_3O_4 preserved the spinel structure of Mn_3O_4 with the predominantly exposed (103) plane, as shown by transmission electron microscopy (TEM) images and X-ray diffraction (XRD) patterns **(Figure 1b-d)**.[15] Energy dispersive spectroscopy (EDS) mapping images show uniform distribution of Co and N elements over CoN_1O_2/Mn_3O_4 particles (**Figure 1c**).[16] We further identified Co atoms on the surface of CoN_1O_2/Mn_3O_4 in high-angle annular dark-field scanning transmission electron microscopy (HAADF-STEM) images (**Figure 1e-g**), in which isolated metal sites with increased contrast in the selected area of the intensity surface plots can be observed.[17] The shrinkage of the spacing between adjacent metal atoms also corroborates the precise replacement of Mn sites by Co atoms, because the radius of Co^{2+} (tetrahedral, ~72 pm) is slightly smaller than that of Mn^{2+} (tetrahedral, ~80 pm).[18] In addition, the morphology and crystal structure of Co/Mn_3O_4 resembled CoN_1O_2/Mn_3O_4 (**Figure S2**), and Co also atomically dispersed over Mn_3O_4 surface (**Figure S3**). Thus, we successfully anchored the single Co atoms on the Mn_3O_4 surface to obtain CoN_1O_2/Mn_3O_4 and Co/Mn_3O_4 SACs.

We evaluated the possible changes of Mn sites in Mn_3O_4 during the synthesis. The X-ray photoelectron spectroscopy (XPS) spectra of Mn 3s in CoN_1O_2/Mn_3O_4 revealed that the multiple splitting energies were consistent with typical spinel Mn_3O_4 (ΔE = 5.6 eV, **Figure 2a**), indicating that the introduction of Co and N had negligible impact on the oxidation states of Mn.[19] However, the Mn K-edge extended X-ray absorption fine structure (EXAFS) spectrum of CoN_1O_2/Mn_3O_4 **(Figure 2b)** shows that the remarkable peak near 1.5 Å (mainly representing Mn-O scattering) had a decreased intensity and a slightly left shifted position in comparison to that of the pristine Mn_3O_4, indicating the disorder of the coordination atoms in the first shell of Mn increased.[20] Thus, the first-shell coordination of Mn in the Mn_3O_4 was disturbed after anchoring the CoN_1O_2 configuration.

The coordination environment and the valence state of Co sites were subsequently investigated. The absence of a metallic Co-Co scattering path (2.15 Å) in the Co K-edge EXAFS spectra of both Co/Mn_3O_4 and CoN_1O_2/Mn_3O_4, verifies the atomic dispersion of Co (**Figure 2d**). The first peak of CoN_1O_2/Mn_3O_4 located at 1.53 Å, between the backscattering of Co-N (1.47 Å) and Co-O (1.65 Å), is broad and asymmetric, suggesting the existence of Co-N and Co-O dual coordination in CoN_1O_2/Mn_3O_4.[1c, 20b, 21] Different from CoN_1O_2/Mn_3O_4, the main peak of Co/Mn_3O_4 at ~1.64 Å can be well attributed to Co-O coordination. The wavelet transformation (WT) contour plots of

10.1002/anie.202303267

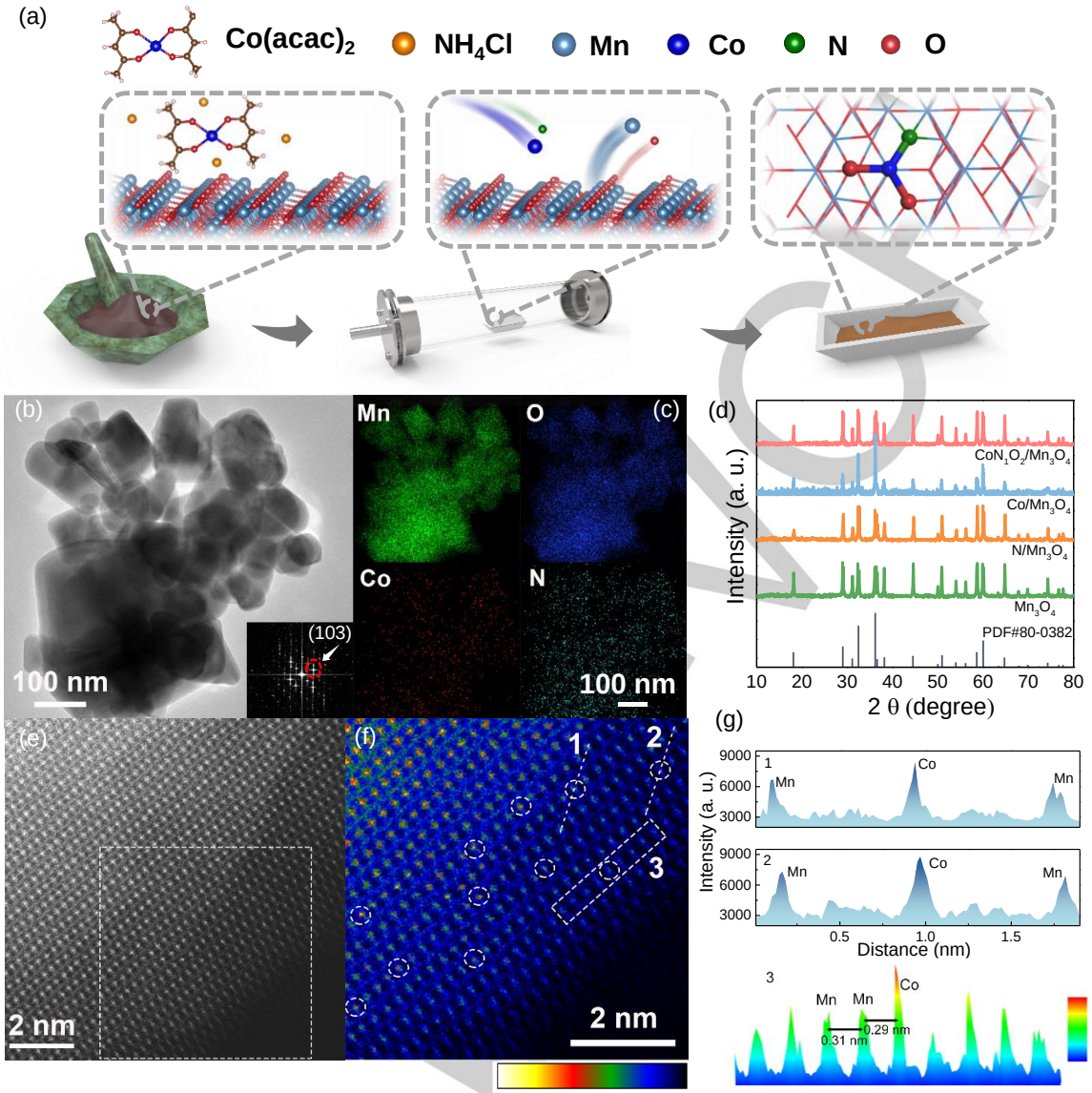

Figure 1. (a) Schematic illustration of CoN_1O_2/Mn_3O_4 synthesis; (b) TEM and (c) EDS mapping images of CoN_1O_2/Mn_3O_4; inset of b is the fast Fourier transform pattern; (d) XRD profiles of catalysts; (e) HAADF-STEM image of CoN_1O_2/Mn_3O_4; (f) Enlarged view of the marked region in (e); and (g) intensity of surface plots from the selected regions in (f).

CoN_1O_2/Mn_3O_4 display an intensity maximum at 4.56 $Å^{-1}$, which is between CoPc (4.42 $Å^{-1}$) and CoO (4.62 $Å^{-1}$), further corroborating the coexistence of Co-N and Co-O paths (**Figure 2h**).[16, 21c, 22] The presence of Co-N bonds in CoN_1O_2/Mn_3O_4 was also supported by the peak at 399.2 eV in the N 1s deconvolution spectrum (**Figure S4**).[23] The WT plots also excludes the formation of CoO in CoN_1O_2/Mn_3O_4, because the second coordination shell of Co in CoN_1O_2/Mn_3O_4 is clearly different from CoO: Co-(N/O)-Mn and Co-(O)-Co configurations in CoN_1O_2/Mn_3O_4 and CoO show intensity maxima at 7.22 and 6.22 $Å^{-1}$, respectively (**Figure 2h**). As nicely fitted by the optimized models with EXAFS spectra (**Table S1, Figure 2f and S5**), the coordination numbers in the first shell of Co were calculated to be 3.1 ± 0.1 and 2.9 ± 0.2 for CoN_1O_2/Mn_3O_4 and Co/Mn_3O_4, respectively. Furthermore, the distance of the Co-(N/O)-Mn bond in the second shell of CoN_1O_2/Mn_3O_4 was consistent with that of the Co_{Td}-(O)-$TM_{Td/Oh}$ bond in Co_3O_4 (≈3.0 Å), illustrating that Co occupies the tetrahedral site of the spinel structure (**Figure 2e**). The valence state of Co in CoN_1O_2/Mn_3O_4 was estimated to be ~+2.26 based on linear fitting results from the Co K-edge X-ray absorption near edge structure (XANES) spectra (**Figure 2c**). This verifies that Co tended to occupy the tetrahedral sites in the spinel crystal, at which its oxidation state is +2.[24] Since elemental analyses by XPS and TEM-EDS revealed that the atomic ratio of Co to N in CoN_1O_2/Mn_3O_4 was close to 1 (**Table S2, S3**), the local structure of Co sites in CoN_1O_2/Mn_3O_4 was assumed to be an isolated Co

10.1002/anie.202303267

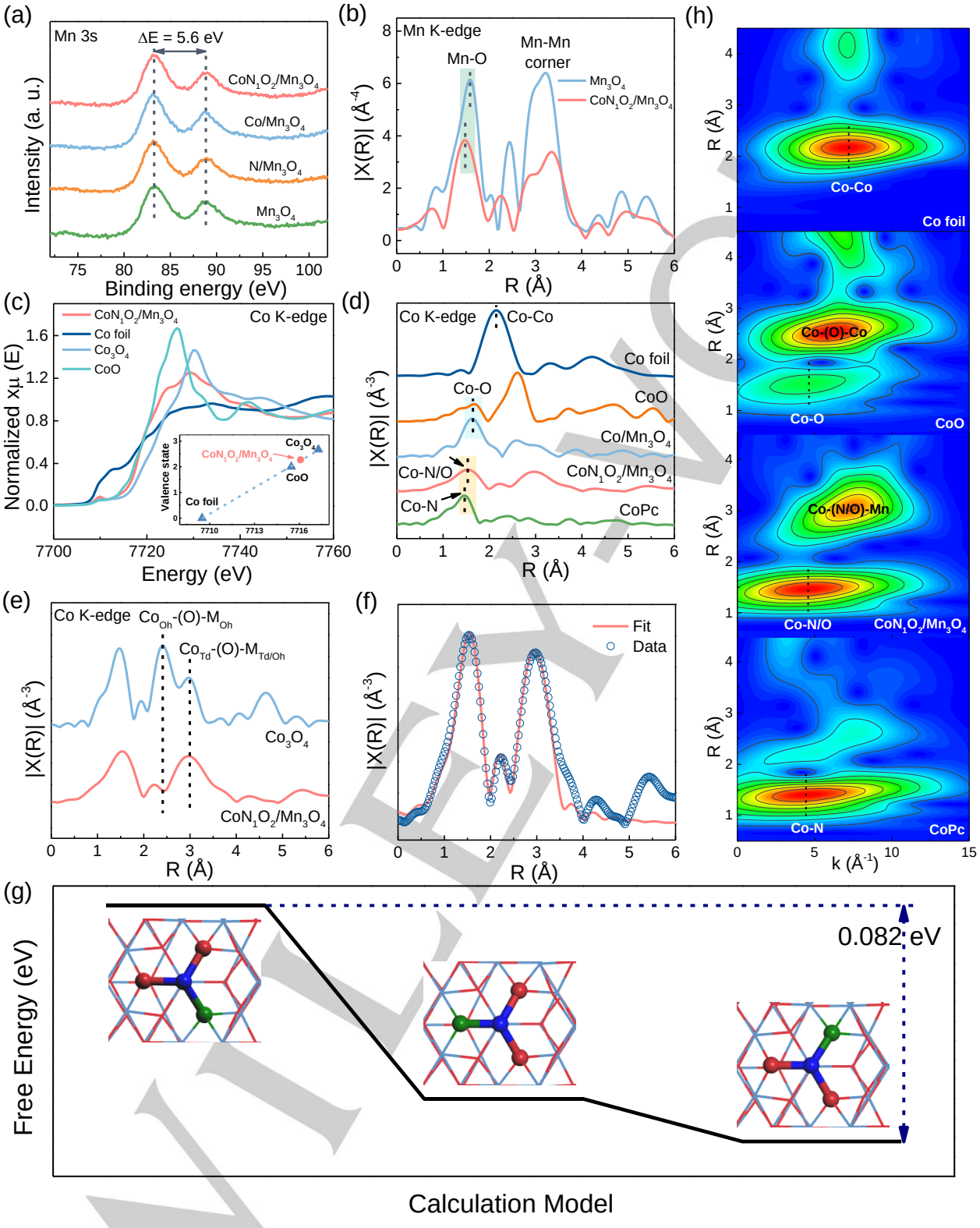

Figure 2. (a) Mn 3s XPS spectra of catalysts; (b) K-edge EXAFS spectra in R-space of Mn; (c) Normalized Co K-edge XANES spectra; (d) and (e) Fourier-transformed k^2-weighted EXAFS spectra of CoN_1O_2/Mn_3O_4, Co/Mn_3O_4 and references in R space; (f) Co K-edge EXAFS (points) and fit (line) for the CoN_1O_2/Mn_3O_4, shown in k^2-weighted R-space; (g) The structural models of three CoN_1O_2 isomer and their free energies calculated by DFT; (h) Wavelet transformation for the k^2-weighted EXAFS signal of CoN_1O_2/Mn_3O_4 and reference samples.

atom coordinated with one nitrogen and two oxygen atoms (CoN_1O_2). We subsequently constructed three isomer CoN_1O_2 models on Mn_3O_4 surface with different relative positions of Co and N atoms and performed density functional theory (DFT) calculation to obtain the most favorable configuration that had the lowest free energy (**Figure 2g**).

The antibiotic sulfamethoxazole (SMX), a recalcitrant micropollutant frequently detected in water, was used to evaluate the catalytic performance of CoN_1O_2/Mn_3O_4 for PMS activation.[25] Optimization experiments of Co doping amount indicated that the catalyst with 0.8 wt% Co had the best performance for SMX removal (**Figure S7**), and excessive Co doping led to clustering and a decrease in catalytic performance (**Figure S8-S9**). The catalysts with similar crystal structures (all conforming to Mn_3O_4) differed greatly in performance for PMS activation, with CoN_1O_2/Mn_3O_4 showing the most prominent catalytic activity, achieving 100% SMX removal within 30 min (**Figure 3a**). In contrast, the control samples (Mn_3O_4, Co/Mn_3O_4 and N/Mn_3O_4), PMS alone and adsorption by CoN_1O_2/Mn_3O_4 displayed negligible SMX removal (**Figure 3a, Figure S10**). To identify the active sites in CoN_1O_2/Mn_3O_4, NaF and KSCN (2 mM) were employed to shield Mn and Co sites, respectively.[26] NaF has negligible impact on SMX degradation (**Figure 3b**), while KSCN almost completely suppressed SMX removal due to the strong coordination between Co sites and SCN^- anions. Therefore, Co sites were the dominant active sites for PMS activation rather than Mn sites, and the catalytic inertness of Co/Mn_3O_4 can also exclude the contribution of Mn sites located in the second coordination shell to the PMS activation on the Co sites.

SMX degradation rate constants were normalized per mole of Co sites ($k_{per\text{-}site}$) to evaluate the activity of different catalysts.[1c, 13b] CoN_1O_2/Mn_3O_4 had the highest $k_{per\text{-}site}$ value (**Figure 3c**), which was 3.2, 5.9, 17.9 and 14.7 times higher than CoN_4-C, CoO, Co_3O_4 and Co/Mn_3O_4, respectively. The specific apparent rate constants (k_{SA}), which take into account the concentration ratios of pollutant to oxidant and specific surface areas (eq. S2), were used to assess the intrinsic activity of the catalysts, and CoN_1O_2/Mn_3O_4 was higher than that of reported Co-based catalysts (**Table S5**). The leached Co ions concentrations from CoN_1O_2/Mn_3O_4 (0.06 ppm) were well below the discharge standard (1.0 mg/L, GB 25467-2010) in China,[27] and were less than 0.001 ppm after the third cycle (**Figure 3d**). SMX removal by the dissolved Co ions was negligible (6.2% within 30 min, **Figure S11**), ruling out the contribution of homogeneous Co^{2+}. After six consecutive cycles, SMX removal within 30 min still reached 85% (**Figure 3d**), verifying the robustness of CoN_1O_2/Mn_3O_4. Different water matrices (deionized water, lake water, tap water), inorganic anions (Cl^-, HCO_3^-, NO_3^-) and organic matter (humic acid) showed insignificant impact on SMX removal (**Figure 3e, Figure S12**), indicating that CoN_1O_2/Mn_3O_4-activated PMS had high resistance to common coexisting inhibitory substances in real waters.[1a]

We further identified the active species in the CoN_1O_2/Mn_3O_4-PMS system. Tert-butyl alcohol (TBA), methanol (MeOH), 2,2,6,6 tetramethyl-4-piperidinyl (TEMP), and dimethyl sulfoxide (DMSO) were used as the scavengers of •OH, $SO_4^{\bullet-}$, $^1O_2$ and HVMO species, respectively.[1a, 28] Both TBA and TEMP did not significantly inhibit SMX degradation (**Figure 3f**), indicating the negligible contribution of •OH and $^1O_2$. MeOH, a conventional quencher for radicals (such as $SO_4^{\bullet-}$ or •OH), inhibited SMX removal, which at first glance suggests participation by $SO_4^{\bullet-}$ in SMX removal. However, if $SO_4^{\bullet-}$ were the main active species during PMS activation by CoN_1O_2/Mn_3O_4, considering the high reaction rate constant between $SO_4^{\bullet-}$ and TBA ($k_{SO_4^{\bullet-},TBA} = 4.0 \times 10^5\ M^{-1}s^{-1}$), the much higher TBA than SMX concentration would result in scavenging of considerable fraction of $SO_4^{\bullet-}$.[29] The percentage of $SO_4^{\bullet-}$ scavenged by TBA in the total produced $SO_4^{\bullet-}$ (P, %) can be calculated according to **eq. 1**.

$$P\ (\%) = \frac{\left(k_{SO_4^{\bullet-},TBA}[TBA]\right)}{\left(k_{SO_4^{\bullet-},TBA}[TBA] + k_{SO_4^{\bullet-},SMX}[SMX]\right)} \times 100 \qquad \textbf{(eq. 1)}$$

where $k_{SO_4^{\bullet-},TBA}$ and $k_{SO_4^{\bullet-},SMX}$ are the second-order rate constants for the reactions between $SO_4^{\bullet-}$ with TBA and SMX, respectively (see **Table S4** for details).[29] At 2 ppm SMX, 100 mM TBA and 500 mM TBA can theoretically scavenge 30.2% and 68.4% $SO_4^{\bullet-}$, respectively. However, TBA exerted relatively low inhibition of SMX removal at all tested concentrations (see **Figure S13**), inferring that the contribution of $SO_4^{\bullet-}$ to SMX degradation was negligible. Thus, the inhibition from methanol addition may be attributed to the competing reaction between methanol and other non-radical species.[2]

Removal of typical radical scavengers like nitrobenzene (NB) and benzoic acid (BA) was also insignificant (**Figure S14**) in the CoN_1O_2/Mn_3O_4-PMS system. The electron paramagnetic resonance (EPR) spectra with 5,5-dimethyl-1-pyrrolidine-N-oxide (DMPO) as the spin trapper shows no signal of DMPO-•OH and DMPO-$O_2^{\bullet-}$, further ruling out the contribution of •OH and $O_2^{\bullet-}$ (**Figure 3g, Figure S15**).[30] The seven-line spectrum in the EPR spectra can be attributed to 5,5-dimethyl-1-pyrrolidone-2-oxyl (DMPOX) (**Figure 3g**), the direct oxidation product of DMPO via a non-radical pathway.[1a] The intensities of TEMP-$^1O_2$ triplet signals in both PMS alone and CoN_1O_2/Mn_3O_4-PMS system were comparable. The participation of $^1O_2$ can also be excluded since its lifetime in D_2O (68 ± 1 μs) is approximately 18-time longer than

10.1002/anie.202303267

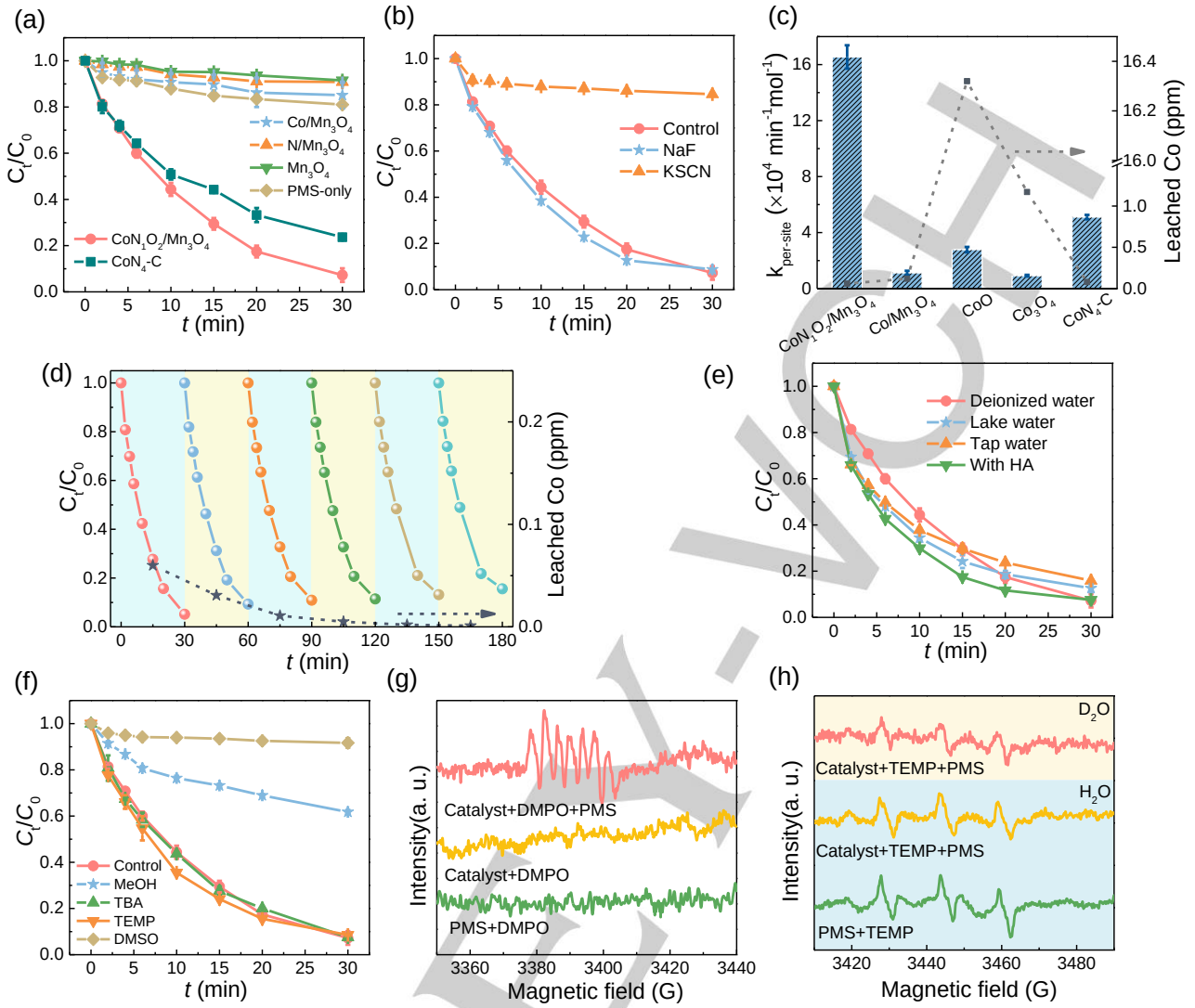

Figure 3. (a) SMX removal efficiency in different catalyst/PMS systems; (b) The quenching experiments to prove Co and Mn active sites; (c) Norm alized Co-site activity ($k_{per-site}$) and leached Co ions for the catalysts, commercial Co oxides, and common Co-SACs (CoN_4-C configuration); (d) Recycle tests and (e) Anti-interference ability of CoN_1O_2/Mn_3O_4; (f) Quenching experiments; (g, h) EPR spectra of different systems. Experiment conditions: [catalysts] = 0.2 g/L, [PMS] = 0.2 mM, [SMX] = 2 ppm, [NaF] = [KSCN] = [DMSO] = 2 mM, [MeOH] = [TBA] = 100 mM, [TEMP] = 0.14 mM, pH = 6.0.

in H_2O (3.7 ± 0.4 μs). The D_2O solvent did not accelerate the SMX degradation or enhance the TEMP-$^1O_2$ triplet signals (**Figure 3h, Figure S16**), but instead exhibited a slight inhibitory effect, which may be arisen from the atomic exchange effect between the H atom in the hydroxyl group of PMS and D_2O.[31] The possibility of the electron transfer pathway, which frequently appeared during PMS activation by carbonaceous catalysts, was also eliminated, because significant PMS decay was observed in the presence or absence of SMX (see **Figure S17**).[32]

As the addition of DMSO into the CoN_1O_2/Mn_3O_4-PMS system resulted in the complete stagnation of SMX degradation (**Figure 3f, Figure S18-19**), we postulate that high-valent Co species like Co^{IV}=O are the dominant reactive species. This was corroborated by the detection of methyl phenyl sulfone ($PMSO_2$) during methyl phenyl sulfoxide (PMSO) oxidation (**Figure 4a**), which infers an oxygen atoms transfer (OAT) reaction that is frequently used to prove the HVMO generation.[2, 27] In contrast to Co/Mn_3O_4-PMS, which only consumed minor PMSO via the direct PMS oxidation, much more PMSO consumption and $PMSO_2$ production were observed in the CoN_1O_2/Mn_3O_4-PMS system, and the percentage of PMSO conversion into $PMSO_2$ was approximately 100% throughout the degradation (**Figure 4b**), which strongly suggests the dominant role of Co^{IV}=O species during PMS activation.[2] The indicative products in the $H_2{}^{18}O$ matrix was determined to provide further evidence, because Co^{IV}=O tends to undergo oxygen atom exchange with the solvent

10.1002/anie.202303267

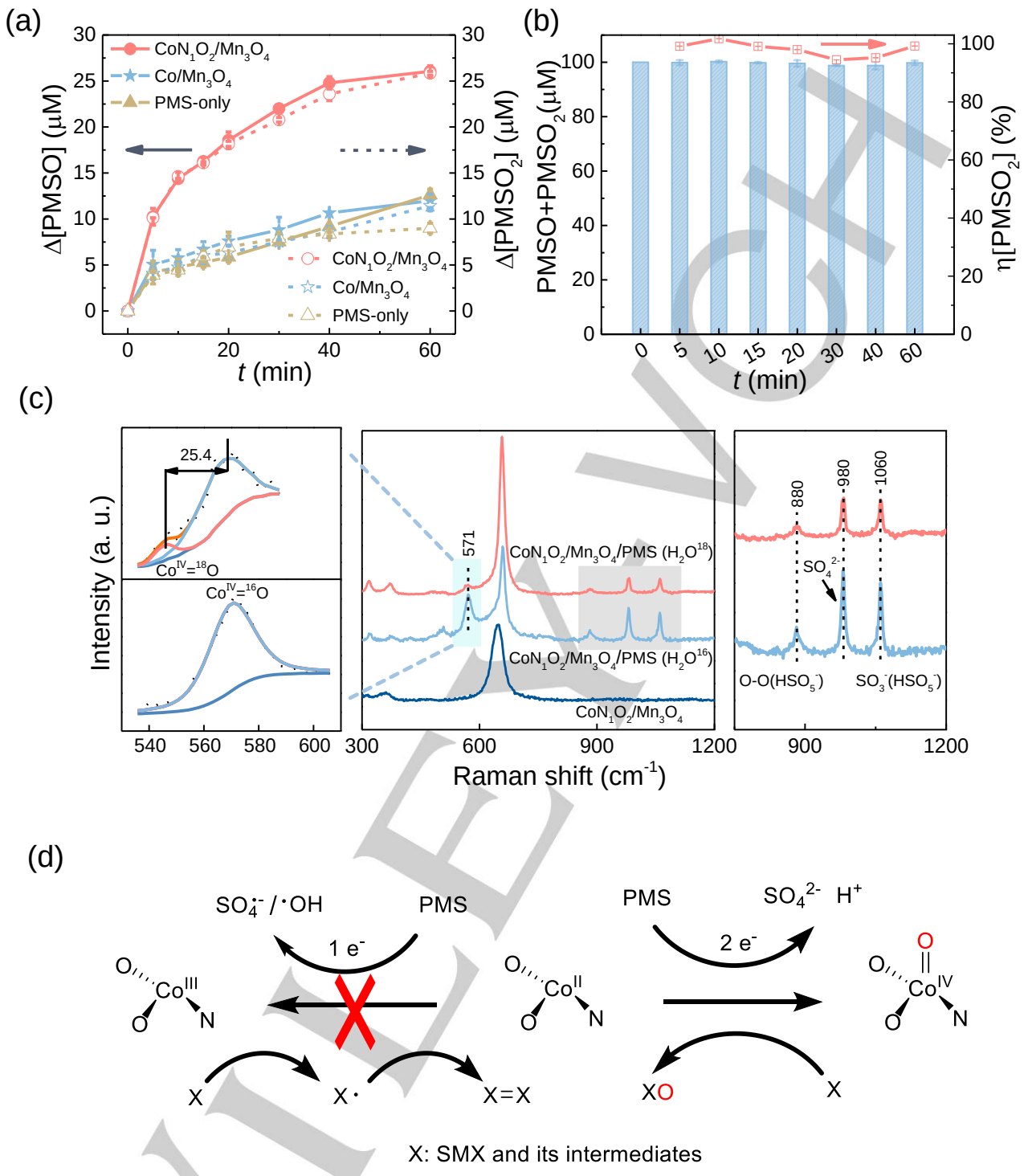

Figure 4. (a) PMSO loss and $PMSO_2$ production in different systems; (b) Sum of PMSO and $PMSO_2$ and the corresponding η($PMSO_2$) at different reaction time; (c) In-situ Raman spectra of CoN_1O_2/Mn_3O_4 activated PMS in $H_2{}^{16}O/H_2{}^{18}O$ matrix; (d) Schematic representation of the pathways for OAT and contaminant degradation. Experiment conditions: [catalysts] = 0.2 g/L, [PMS] = 0.2 mM, $[PMSO]_0$ = 0.1 mM, pH = 6.0.

(water).[33] As expected, by replacing with $H_2{}^{18}O$ matrix, the extracted ion chromatogram (EIC, **Figure S20**) from UPLC-QTOF-MS analysis exhibited two significant peaks at m/z 157.0311 and m/z 159.0351, corresponding to $PMS^{16}O^{16}O$ and $PMS^{16}O^{18}O$, respectively.[33b, 34] Thus, the formation of ^{18}O-labeled $PMSO_2$ provides conclusive evidence for Co^{IV}=O generation.

In-situ Raman spectra also captured the presence of Co^{IV}=O in CoN_1O_2/Mn_3O_4-PMS system. During PMS activation, the emerging Raman peak at 571.0 cm^{-1} was attributed to Co^{IV}=O,

which shifted to 545.6 cm^{-1} when $H_2{}^{16}O$ was replaced by $H_2{}^{18}O$ (see **Figure 4c**). Such redshift was also observed in the isotopic labelling experiments for CoO_2. The oxygen isotopic shift (25.4 cm^{-1}) from the exchange of individual O atom approaches the reported value (26.0 cm^{-1}) of Co^{IV}=O. Therefore, we can reasonably ascribe the Raman peaks at 571.0 cm^{-1} and 545.6 cm^{-1} to $Co^{IV}={}^{16}O$ and $Co^{IV}={}^{18}O$, respectively.[35]

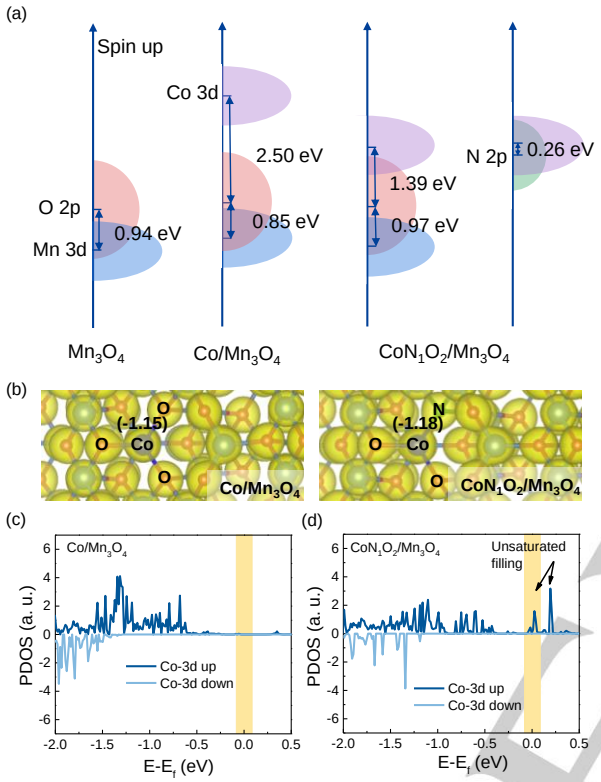

Figure 5. (a) Schematic representation of TM 3d-O/N 2p overlap for CoN_1O_2/Mn_3O_4; (b) The corresponding charge-density wave of Co/Mn_3O_4 and CoN_1O_2/Mn_3O_4 (isosurface level is 0.1 e/Å^3), and the Bader charges of Co atoms in Co/Mn_3O_4 and CoN_1O_2/Mn_3O_4. PDOS of the Co 3d states in Co/Mn_3O_4 (c) and CoN_1O_2/Mn_3O_4 (d).

The CoN_1O_2 configuration enables a Co^{IV}=O-dominant oxidation mechanism upon PMS activation, which differs from the catalytic PMS oxidation mechanisms of most cobalt oxides (radical-dominant) and CoN_4-C SACs ($^1O_2$-dominant).[1b, 4, 27, 36] To clarify the formation of Co^{IV}=O, we analyzed the elemental valence changes of CoN_1O_2/Mn_3O_4 by XPS. After PMS activation, the ΔE value of Mn 3s XPS spectrum in CoN_1O_2/Mn_3O_4 remained at 5.6 eV (**Figure S21**), and the lattice oxygen content was also virtually constant (see **Figure S22**), demonstrating the stability of the substrate and ruling out the electronic interaction between Co-Mn.[37] The Co (III) contents reduced after PMS activation, negating single-electron PMS activation that normally was accompanied by the conversion of Co (II) to Co (III) (**Figure S23**). Thus, Co^{IV}=O must originate from Co (II) via two-electron transfer, whereby the PMS is chemically bound to Co (II) sites, inducing the formation of Co^{IV}=O species on the catalyst surface.

Figure 5a illustrates the O/N 2p band and Co/Mn 3d band (relative to E_f) derived from the projected density of states (PDOS) of catalysts. When Co substitutes for Mn (II) and the coordination atoms of Co are only O atoms, the Co d-band and O p-band are far apart (2.50 eV). However, when N is introduced to coordinate with Co, the energy difference between the Co d-band and O p-band is dramatically reduced to 1.39 eV, implying that the incorporation of nitrogen strengthens the hybridization of Co-O bonds.[24a, 37-38]

Charge density analysis provides additional evidence (**Figure 5b**) for the Co sites in CoN_1O_2/Mn_3O_4 exhibit significant electronic delocalization accompanied by the asymmetric electronic distribution. Compared with Co/Mn_3O_4, the reduced Bader charge of the Co atom in CoN_1O_2/Mn_3O_4 indicates that partial electrons from the Co central were extracted after nitrogen introduction. Correspondingly, the partial spin-up orbitals of Co 3d in CoN_1O_2/Mn_3O_4 are unoccupied (**Figure 5c-d**), which further corroborates the unsaturated electronic filling of Co 3d orbitals. The reduced electron density is also proved by the higher binding energy of Co 2p in CoN_1O_2/Mn_3O_4 than that in Co/Mn_3O_4 (**Figure S6**).[9a, 39] Electrochemical experiments further verified the rapid electron transfer between Co sites and PMS molecules. The in-situ open-circuit potentials (OCP) of CoN_1O_2/Mn_3O_4-activated PMS system significantly increased from 0.034 V of Co/Mn_3O_4 to 0.11 V.[1a] Meanwhile, in the current-time test, significant cathodic current immediately emerged when PMS was injected into the CoN_1O_2/Mn_3O_4 system (**Figure S24-S25**). In conclusion, the N coordination in CoN_1O_2/Mn_3O_4 leads to significant electronic delocalization at Co sites, thereby reducing the electronic filling of the Co 3d orbitals, which is crucial for triggering the Co^{IV}=O species generation via PMS activation.

We further compared the adsorption and activation of PMS over CoN_1O_2/Mn_3O_4 and Co/Mn_3O_4 by DFT calculation. In contrast to the non-spontaneous adsorption of PMS on Co/Mn_3O_4 surface (E_{ads} > 0.6 eV, **Figure. 6a**), PMS (HO-OSO_3^-) was chemically bound to the Co sites on CoN_1O_2/Mn_3O_4 spontaneously by one peroxyl oxygen in a terminal end-on mode with a large negative adsorption energy (E_{ads} < -0.7 eV). The energy evolution of the critical intermediates during PMS activation by the catalysts with or without N coordination was compared (**Figure 6b-c**). First, PMS adsorbs on Co sites to form Co-O(H)OSO_3^- (**II**), and then dissociates into Co-$OOSO_3$ (**III**) by deprotonation. Eventually, the O-O bond is broken to generate Co^{IV}=O (**IV**) and SO_4^{2-} anions. The energy potential of CoN_1O_2/

10.1002/anie.202303267

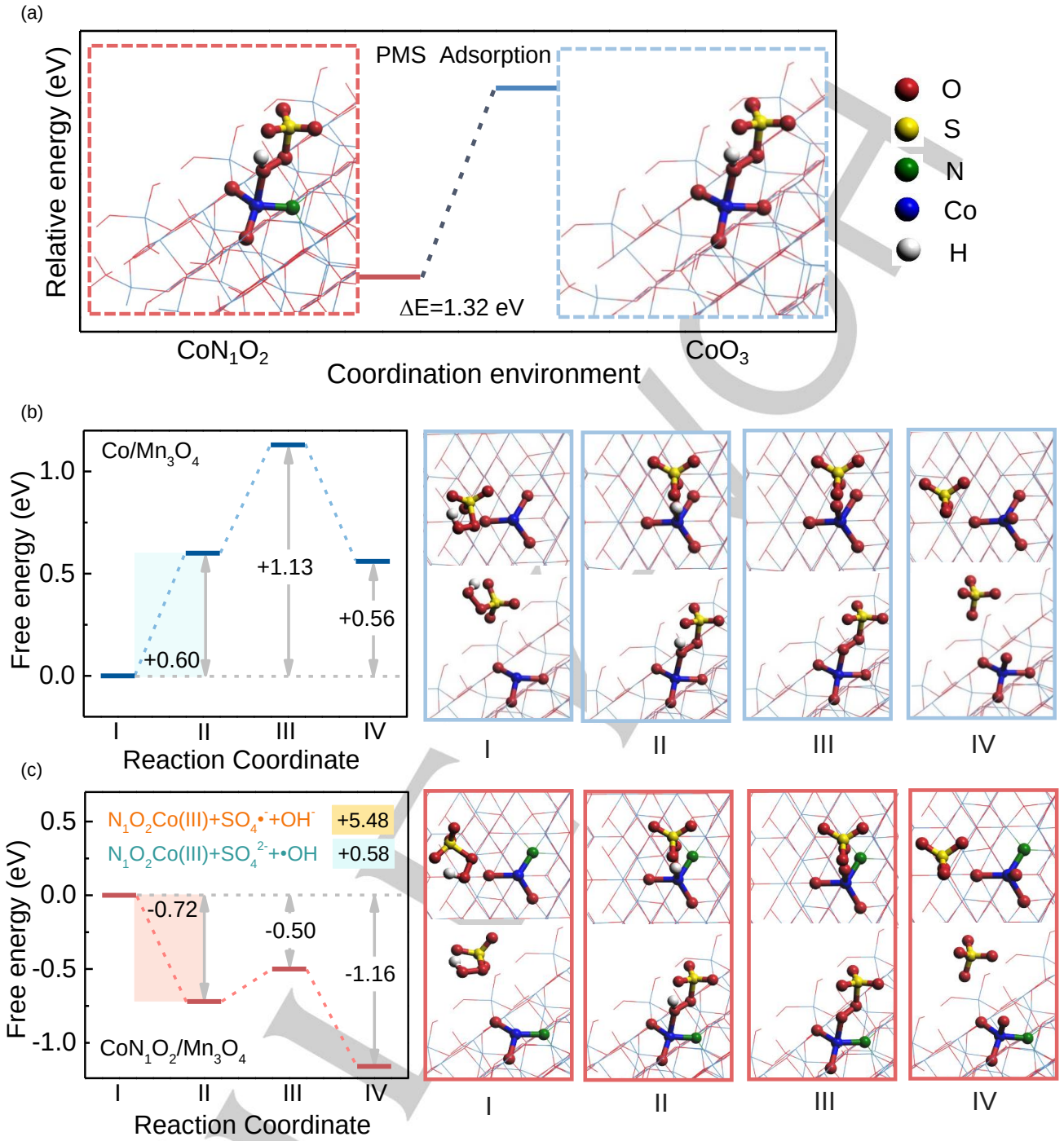

Figure 6. Theoretical calculations of PMS adsorption and activation on Co/Mn_3O_4 and CoN_1O_2/Mn_3O_4; (a) The adsorption energy of PMS (HSO_5^-) on CoN_1O_2 and CoO_3 sites. Energy profiles of Co^{IV}=O species formation for Co/Mn_3O_4 (b) and CoN_1O_2/Mn_3O_4 (c) by PMS activation (Right side: Top view (top) and side view (bottom) of the intermediate structure).

Mn_3O_4 system is obviously favorable to produce Co^{IV}=O (-1.16 eV), but infeasible to produce •OH (+0.58 eV) and $SO_4^{\bullet-}$ (+5.48 eV), which is consistent with the proved non-radical pathway of CoN_1O_2/Mn_3O_4-PMS system. Compared to the high energy barriers faced by Co/Mn_3O_4 throughout **I-IV**, the formation of Co^{IV}=O species during PMS activation by CoN_1O_2/Mn_3O_4 is also thermodynamically more feasible.[40] According to the energy differences, the thermodynamic rate-determining step (RDS) in the Co/Mn_3O_4-PMS system is Co-O(H)OSO_3^- formation (**I to II**), but changes into the deprotonation of the adsorbed PMS (**II to III**) in the CoN_1O_2/Mn_3O_4-PMS system, which may be the fundamental reason for the efficient generation of Co^{IV}=O during

PMS activation.[41] The above calculations indicate that the Co-SAC with N_1O_2 coordination is an effective catalyst for PMS activation to produce Co^{IV}=O, and N doping reduces the high occupancy of the Co 3d orbitals by inducing electronic delocalization at Co sites, which is thermodynamically more favorable for the occurrence of PMS activation with Co^{IV}=O species generation. Furthermore, we synthesized CoN_1O_2/Fe_3O_4 with the same method for CoN_1O_2/Mn_3O_4, and interestingly found this CoN_1O_2/Fe_3O_4 sample also displayed a high activity in PMS activation (**Figure S26**), suggesting the generality of our concept. Thus, the enhanced catalytic performance of CoN_1O_2/Mn_3O_4-PMS was arisen from the selective generation of Co^{IV}=O species, whose dominant role was confirmed by in-situ Raman, selective oxidation of PMSO into $PMSO_2$, isotopic labelling experiments and DFT calculations.

The transformation products (TPs) of SMX degradation in CoN_1O_2/Mn_3O_4-PMS system were identified by UPLC-QTOF-MS (ESI, positive mode), and the possible degradation pathway (**Figure S27-28**) was proposed. Different from the radical-dominant pathways, Co^{IV}=O oxidized aniline rings via OAT and induced N-S bonds broken, as abundant OAT products were found during SMX degradation.[42] For example, an oxygen transferred to aniline rings and formed an intermediate containing -NHOH group (TP-270), which in turn further produced TP-284 with $-NO_2$ group (**Figure S27**). TP-114 and TP-130 were also produced by typical OAT reactions in Co^{IV}=O oxidation, and nitrobenzene (TP-124) accumulated in the solution due to its sluggish oxidation by HVMO species, which was also evidenced by the negligible removal of nitrobenzene in CoN_1O_2/Mn_3O_4-PMS system (**Figure S14**).[43]

Furthermore, highly toxic azo products generated via the coupling of N-centered radicals, readily detected in the radical-dominated system, were not detected in the CoN_1O_2/Mn_3O_4 activated PMS system.[44] Acute toxicity, developmental toxicity and bioaccumulation factors of TPs were evaluated by quantitative structure-activity relationship (QSAR) models, and significant detoxification was achieved (**Figure S29**).[8, 44] The schematic diagram of PMS activation and pollutant degradation is illustrated in **Figure 4d**. In summary, unlike radicals, Co^{IV}=O oxidizes pollutants via OAT to produce the intermediate products with effectively reduced toxicity.

Conclusion

A CoN_1O_2 configuration on the Mn_3O_4 surface was developed to efficiently activate PMS to selectively produce Co^{IV}=O reactive species. The coordination structure of CoN_1O_2/Mn_3O_4 was determined by characterization and theoretical calculations. Compared with commercial cobalt oxides and Co-N-C materials, CoN_1O_2/Mn_3O_4 combines the advantages of high-efficiency PMS activation, high stability and less metal dissolution. Benefited from the selective production and strong oxidation potential of Co^{IV}=O species, CoN_1O_2/Mn_3O_4 has outstanding intrinsic activity. Mechanistic analysis verified that the N introduction in the CoN_1O_2 unit results in the electronic delocalization at Co sites, reducing the electronic filling of the Co 3d orbitals, thus facilitating the PMS adsorption on the Co sites, and the subsequent formation of Co^{IV}=O species via two-electron activation of PMS. The intermediates proved that OAT is the main pathway for the oxidation of organic pollutants. This HVMO-dominated system has great resistance to interference and low product toxicity. These findings provide a novel design principle for transition metal oxide-based SACs and a valuable exploration of the non-radical activation mechanism of PMS at the molecular level.

Acknowledgements

Financial supports from the National Natural Science Foundation of China (nos. 52070128, 21876108, 22106104, and 21936003) and the NSF ERC on Nanotechnology-Enabled Water Treatment (no. EEC-1449500) are gratefully acknowledged. We also thank the BL 14W beamline at the Shanghai Synchrotron Radiation facility (SSRF, 2021-SSRF-PT-016444) and the Student Innovation center at Shanghai Jiao Tong University.

Keywords: Single-atom catalysts • Electron Delocalization • High-Valent Cobalt • Peroxymonosulfate • Pollutants

References

[1] a)Y. Bao, C. Lian, K. Huang, H. Yu, W. Liu, J. Zhang, M. Xing, *Angew Chem Int Ed Engl* **2022**, e202209542. *Angew. Chem.*, **2022**, *134*(42), e202209542; b)X. Mi, P. Wang, S. Xu, L. Su, H. Zhong, H. Wang, Y. Li, S. Zhan, *Angew Chem Int Ed Engl* **2021**, *60*, 4588-4593. *Angew. Chem.*, **2021**, *133*(9), 4638-4643; c)Z. Wang, E. Almatrafi, H. Wang, H. Qin, W. Wang, L. Du, S. Chen, G. Zeng, P. Xu, *Angew Chem Int Ed Engl* **2022**, *61*, e202202338. *Angew. Chem.*, **2022**, *134*(29), e202202338

[2] Y. Zong, X. Guan, J. Xu, Y. Feng, Y. Mao, L. Xu, H. Chu, D. Wu, *Environ Sci Technol* **2020**, *54*, 16231-16239.

[3] P. Hu, M. Long, *Applied Catalysis B: Environmental* **2016**, *181*, 103-117.

[4] Y. Yao, C. Wang, X. Yan, H. Zhang, C. Xiao, J. Qi, Z. Zhu, Y. Zhou, X. Sun, X. Duan, J. Li, *Environ Sci Technol* **2022**, *56*, 8833-8843.

[5] a)K. J. K. Koola J D, *The Journal of Organic Chemistry* **1987**, *52*, 4545-4553. ; b)R. Su, N. Li, Z. Liu, X. Song, W. Liu, B. Gao, W. Zhou, Q. Yue, Q. Li, *Environ Sci Technol* **2023**, *57*, 1882-1893.

[6] a)K. Qian, H. Chen, W. Li, Z. Ao, Y. N. Wu, X. Guan, *Environ Sci Technol* **2021**, *55*, 7034-7043. ; b)Z. Wang, W. Qiu, S. Y. Pang, Q. Guo, C. Guan, J. Jiang, *Environ Sci Technol* **2022**, *56*, 1492-1509. ; c)O. Pestovsky., A. Bakac., *Inorg. Chem.* **2006**, *45*, 814-820.

[7] a)M. Kondo, H. Tatewaki, S. Masaoka, *Chem Soc Rev* **2021**, *50*, 6790-6831. ; b)H. B. Gray, *Chemistry International* **2019**, *41*, 16-19. ; c)V. A. Larson, B. Battistella, K. Ray, N. Lehnert, W. Nam, *Nature Reviews Chemistry* **2020**, *4*, 404-419. ; d)E. Andris, R. Navratil, J. Jasik, M. Srnec, M. Rodriguez, M. Costas, J. Roithova, *Angew Chem Int Ed Engl* **2019**, *58*, 9619-9624. *Angew. Chem.*, **2019**, *131*(28), 9721-9726

[8] B. Liu, W. Guo, W. Jia, H. Wang, S. Zheng, Q. Si, Q. Zhao, H. Luo, J. Jiang, N. Ren, *Water Res* **2021**, *201*, 117313.

[9] a)Y. L. Zhang, B. Liu, Y. K. Dai, Y. F. Xia, P. Guo, Y. Y. Liu, F. Kong, Q. Zhang, L. Zhao, Z. B. Wang, *Advanced Functional Materials* **2022**, *32*, 2209499. ; b)J. R. Winkler, H. B. Gray, in *Molecular Electronic Structures of Transition Metal Complexes I* (Eds.: D. M. P. Mingos, P. Day, J. P. Dahl), Springer Berlin Heidelberg, Berlin, Heidelberg, **2012**, pp. 17-28.

[10] a)F. F. Pfaff, S. Kundu, M. Risch, S. Pandian, F. Heims, I. Pryjomska-Ray, P. Haack, R. Metzinger, E. Bill, H. Dau, P. Comba, K. Ray, *Angew Chem Int Ed Engl* **2011**, *50*, 1711-1715. ; b)B. Wang, Y. M. Lee, W. Y. Tcho, S. Tussupbayev, S. T. Kim, Y. Kim, M. S. Seo, K. B. Cho, Y. Dede, B. C. Keegan, T. Ogura, S. H. Kim, T. Ohta, M. H. Baik, K. Ray, J. Shearer, W. Nam, *Nat Commun* **2017**, *8*, 14839. *PMC5376677*(

[11] a)Y. Xiong, H. Li, C. Liu, L. Zheng, C. Liu, J. O. Wang, S. Liu, Y. Han, L. Gu, J. Qian, D. Wang, *Adv Mater* **2022**, e2110653. ; b)X. Dong, Z. Chen, A. Tang, D. D. Dionysiou, H. Yang, *Advanced Functional Materials* **2022**, *32*, 2111565.

[12] H. Li, K. Gan, R. Li, H. Huang, J. Niu, Z. Chen, J. Zhou, Y. Yu, J. Qiu, X. He, *Advanced Functional Materials* **2022**, *33*, 2208622.

[13] a)J. Song, N. Hou, X. Liu, M. Antonietti, Y. Wang, Y. Mu, *Applied Catalysis B: Environmental* **2023**, *325*, 122368. ; b)X. Liang, D. Wang, Z. Zhao, T. Li, Y. Gao, C. Hu, *Advanced Functional Materials* **2022**, *32*, 2203001. ; c)J. Miao, Y. Zhu, J. Lang, J. Zhang, S. Cheng, B. Zhou, L. Zhang, P. J. J. Alvarez, M. Long, *ACS Catalysis* **2021**, *11*, 9569-9577. ; d)M. Xie, F. Dai, J. Li, X. Dang, J. Guo, W. Lv, Z. Zhang, X. Lu, *Angew Chem Int Ed Engl* **2021**, *60*, 14370-14375. ; e)A. Li, S. Kong, C. Guo, H. Ooka, K. Adachi, D. Hashizume, Q. Jiang, H. Han, J. Xiao, R. Nakamura, *Nature Catalysis* **2022**, *5*, 109-118.

[14] Z. Zhuang, Y. Li, R. Yu, L. Xia, J. Yang, Z. Lang, J. Zhu, J. Huang, J. Wang, Y. Wang, L. Fan, J. Wu, Y. Zhao, D. Wang, Y. Li, *Nature Catalysis* **2022**, *5*, 300-310.

[15] D. M. Robinson, Y. B. Go, M. Mui, G. Gardner, Z. Zhang, D. Mastrogiovanni, E. Garfunkel, J. Li, M. Greenblatt, G. C. Dismukes, *J Am Chem Soc* **2013**, *135*, 3494-3501.

[16] H. Fei, J. Dong, Y. Feng, C. S. Allen, C. Wan, B. Volosskiy, M. Li, Z. Zhao, Y. Wang, H. Sun, P. An, W. Chen, Z. Guo, C. Lee, D. Chen, I. Shakir, M. Liu, T. Hu, Y. Li, A. I. Kirkland, X. Duan, Y. Huang, *Nature Catalysis* **2018**, *1*, 63-72.

[17] W. Qu, X. Liu, J. Chen, Y. Dong, X. Tang, Y. Chen, *Nat Commun* **2020**, *11*, 1532. *PMC7093475*(

[18] a)H. Gu, X. Liu, X. Liu, C. Ling, K. Wei, G. Zhan, Y. Guo, L. Zhang, *Nat Commun* **2021**, *12*, 5422. *PMC8440510*(; b)K. Qi, X. Cui, L. Gu, S. Yu, X. Fan, M. Luo, S. Xu, N. Li, L. Zheng, Q. Zhang, J. Ma, Y. Gong, F. Lv, K. Wang, H. Huang, W. Zhang, S. Guo, W. Zheng, P. Liu, *Nat Commun* **2019**, *10*, 5231. *PMC6863867*(

[19] J. Masa, W. Xia, I. Sinev, A. Zhao, Z. Sun, S. Grutzke, P. Weide, M. Muhler, W. Schuhmann, *Angew Chem Int Ed Engl* **2014**, *53*, 8508-8512.

[20] a)H. Jiang, Z. Wei, L. Ma, Y. Yuan, J. J. Hong, X. Wu, D. P. Leonard, J. Holoubek, J. J. Razink, W. F. Stickle, F. Du, T. Wu, J. Lu, X. Ji, *Angew Chem Int Ed Engl* **2019**, *58*, 5286-5291. *Angew. Chem.*, **2019**, *131*(16), 5340-5345; b)Y. Zhou, S. Sun, S. Xi, Y. Duan, T. Sritharan, Y. Du, Z. J. Xu, *Adv Mater* **2018**, *30*, 1705407.

[21] a)J. Ji, H. Wan, B. Zhang, C. Wang, Y. Gan, Q. Tan, N. Wang, J. Yao, Z. Zheng, P. Liang, J. Zhang, H. Wang, L. Tao, Y. Wang, D. Chao, H. Wang, *Advanced Energy Materials* **2020**, *11*, 2003203. ; b)L. Han, H. Cheng, W. Liu, H. Li, P. Ou, R. Lin, H.-T. Wang, C.-W. Pao, A. R. Head, C.-H. Wang, X. Tong, C.-J. Sun, W.-F. Pong, J. Luo, J.-C. Zheng, H. L. Xin, *Nature Materials* **2022**, *21*, 681–688. ; c)J. Shi, Y. Wei, D. Zhou, L. Zhang, X. Yang, Z. Miao, H. Qi, S. Zhang, A. Li, X. Liu, W. Yan, Z. Jiang, A. Wang, T. Zhang, *ACS Catalysis* **2022**, *12*, 7760-7772.

[22] H. Y. Wang, S. F. Hung, H. Y. Chen, T. S. Chan, H. M. Chen, B. Liu, *J Am Chem Soc* **2016**, *138*, 36-39.

[23] a)A. M. Elshahawy, C. Guan, W. Zang, S. Ding, Z. Kou, S. J. Pennycook, N. Yan, J. Wang, *ACS Applied Energy Materials* **2018**, *2*, 616-626. ; b)K. R. Yoon, C. K. Hwang, S. H. Kim, J. W. Jung, J. E. Chae, J. Kim, K. A. Lee, A. Lim, S. H. Cho, J. P. Singh, J. M. Kim, K. Shin, B. M. Moon, H. S. Park, H. J. Kim, K. H. Chae, H. C. Ham, I. D. Kim, J. Y. Kim, *ACS Nano* **2021**, *15*, 11218-11230.

[24] a)Y. Duan, S. Sun, S. Xi, X. Ren, Y. Zhou, G. Zhang, H. Yang, Y. Du, Z. J. Xu, *Chemistry of Materials* **2017**, *29*, 10534-10541. ; b)Z. Y. Guo, C. X. Li, M. Gao, X. Han, Y. J. Zhang, W. J. Zhang, W. W. Li, *Angew Chem Int Ed Engl* **2021**, *60*, 274-280. *Angew. Chem.*, **2021**, *133*(1), 278-284

[25] a)Y. Peng, G. Xie, P. Shao, W. Ren, M. Li, Y. Hu, L. Yang, H. Shi, X. Luo, *Applied Catalysis B: Environmental* **2022**, *310*, 121345. ; b)Y. Yang, X. Zhang, J. Jiang, J. Han, W. Li, X. Li, K. M. Yee Leung, S. A. Snyder, P. J. J. Alvarez, *Environ Sci Technol* **2022**, *56*, 13-29.

[26] a)L. Jiang, L. Qiu, T. Cen, Y. Y. Liu, X. Peng, Z. Ye, D. Yuan, *Chem Commun (Camb)* **2020**, *56*, 567-570. ; b)W. Wu, Q. Zhang, X. Wang, C. Han, X. Shao, Y. Wang, J. Liu, Z. Li, X. Lu, M. Wu, *ACS Catalysis* **2017**, *7*, 7267-7273.

[27] J. Jiang, Z. Zhao, J. Gao, T. Li, M. Li, D. Zhou, S. Dong, *Environ Sci Technol* **2022**, *56*, 5611-5619.

[28] H. Li, Z. Zhao, J. Qian, B. Pan, *Environ Sci Technol* **2021**, *55*, 6397-6406.

[29] J. Zhu, S. Wang, H. Li, J. Qian, L. Lv, B. Pan, *Water Res* **2021**, *202*, 117397.

[30] H. Li, N. Yuan, J. Qian, B. Pan, *Environ Sci Technol* **2022**, *56*, 4498-4506.

[31] P. Shao, Y. Jing, X. Duan, H. Lin, L. Yang, W. Ren, F. Deng, B. Li, X. Luo, S. Wang, *Environ Sci Technol* **2021**, *55*, 16078-16087.

[32] Y. Gao, Z. Chen, Y. Zhu, T. Li, C. Hu, *Environ Sci Technol* **2020**, *54*, 1232-1241.

[33] a)B. Liu, W. Guo, Q. Si, W. Jia, S. Zheng, H. Wang, Q. Zhao, H. Luo, J. Jiang, N. Ren, *Chemical Engineering Journal* **2022**, *446*, 137277. ; b)B. Liu, W. Guo, H. Wang, S. Zheng, Q. Si, Q. Zhao, H. Luo, N. Ren, *J Hazard Mater* **2021**, *416*, 125679.

[34] M. S. Seo, J. H. In, S. O. Kim, N. Y. Oh, J. Hong, J. Kim, L. Que, Jr., W. Nam, *Angew Chem Int Ed Engl* **2004**, *43*, 2417-2420.

[35] A. Moysiadou, S. Lee, C. S. Hsu, H. M. Chen, X. Hu, *J Am Chem Soc* **2020**, *142*, 11901-11914.

[36] a)C. Song, Q. Zhan, F. Liu, C. Wang, H. Li, X. Wang, X. Guo, Y. Cheng, W. Sun, L. Wang, J. Qian, B. Pan, *Angew Chem Int Ed Engl* **2022**, *61*, e202200406. *Angew. Chem.*, **2022**, *134*(16), e202200406; b)G. Liu, H. Lv, H. Sun, X. Zhou, *Industrial & Engineering Chemistry Research* **2018**, *57*, 2396-2403. ; c)Q. Yi, X. Li, Y. Li, R. Dai, Z. Wang, *ACS ES&T Engineering* **2022**, *2*, 1836-1846. ; d)J. Song, N. Hou, X. Liu, M. Antonietti, P. Zhang, R. Ding, L. Song, Y. Wang, Y. Mu, *Advanced Materials preprint* **2023**, DOI: 10.1002/adma.202209552. ; e)Q. Wang, C. Liu, D. Zhou, X. Chen, M. Zhang, K. Lin, *Chemical Engineering Journal* **2022**, *439*, 135002.

[37] Z. Y. Guo, Y. Si, W. Q. Xia, F. Wang, H. Q. Liu, C. Yang, W. J. Zhang, W. W. Li, *Proc Natl Acad Sci U S A* **2022**, *119*, e2201607119.

[38] S. Sun, Y. Sun, Y. Zhou, S. Xi, X. Ren, B. Huang, H. Liao, L. P. Wang, Y. Du, Z. J. Xu, *Angew Chem Int Ed Engl* **2019**, *58*, 6042-6047.

[39] C. H. Choi, H.-K. Lim, M. W. Chung, G. Chon, N. Ranjbar Sahraie, A. Altin, M.-T. Sougrati, L. Stievano, H. S. Oh, E. S. Park, F. Luo, P. Strasser, G. Dražić, K. J. J. Mayrhofer, H. Kim, F. Jaouen, *Energy & Environmental Science* **2018**, *11*, 3176-3182.

[40] a)N. Wen, Y. Xia, H. Wang, D. Zhang, H. Wang, X. Wang, X. Jiao, D. Chen, *Adv Sci (Weinh)* **2022**, e2200529. ; b)S. Sun, Y. Sun, Y. Zhou, J. Shen, D. Mandler, R. Neumann, Z. J. Xu, *Chemistry of Materials* **2019**, *31*, 8106-8111.

[41] J. Lee, U. von Gunten, J. H. Kim, *Environ Sci Technol* **2020**, *54*, 3064-3081.

[42] a)J. Li, L. Zhao, M. Feng, C. H. Huang, P. Sun, *Water Res* **2021**, *202*, 117463. ; b)Y. Bao, W. D. Oh, T. T. Lim, R. Wang, R. D. Webster, X. Hu, *Water Res* **2019**, *151*, 64-74.

[43] J. Hohenberger, K. Ray, K. Meyer, *Nat Commun* **2012**, *3*, 720.

[44] B. Liu, W. Guo, W. Jia, H. Wang, Q. Si, Q. Zhao, H. Luo, J. Jiang, N. Ren, *Environ Sci Technol* **2021**, *55*, 12640-12651.

10.1002/anie.202303267

WILEY-VCH

RESEARCH ARTICLE

Entry for the Table of Contents

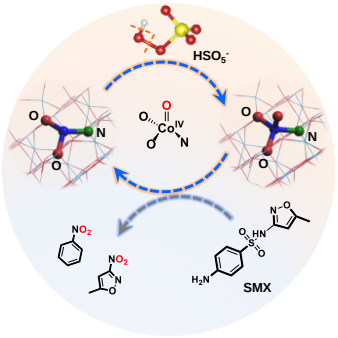

Isolated Co sites with a N_1O_2 coordination pocket were constructed on the surface of Mn_3O_4 to overcome the difficulties in Co^{IV}=O generation during peroxymonosulfate activation. Nitrogen in the asymmetric configuration induces significant electronic delocalization at the Co sites, thus facilitating PMS adsorption, dissociation, and subsequent Co^{IV}=O formation.